

An intramembranous ossification model for the *in-silico* analysis of bone tissue formation in tooth extraction sites

Accepted manuscript for the scientific article with the same name, which was published in the Journal of Theoretical Biology (2016). <https://doi.org/10.1016/j.jtbi.2016.04.023>

Jennifer Paola Corredor-Gómez^{a,b,*}, Andrés Mauricio Rueda-Ramírez^{a,b}, Miguel Alejandro Gamboa-Márquez^{a,b}, Carolina Torres-Rodríguez^{a,c}, Carlos Julio Cortés-Rodríguez^a

^aResearch Group on Biomechanics (GIBM-UN). Mechanical and Mechatronics Engineering. Universidad Nacional de Colombia, Sede Bogotá.

^bAdvanced Technologies Analysis Group (GATAcorp)

^cDepartment of Dentistry. Universidad Nacional de Colombia, Sede Bogotá.

Abstract

The accurate modeling of biological processes allows to predict the spatiotemporal behavior of living tissues by computer-aided (*in-silico*) testing, a useful tool for the development of medical strategies, avoiding the expenses and potential ethical implications of *in-vivo* experimentation. A model for bone healing in mouth would be useful for selecting proper surgical techniques in dental procedures. In this paper, the formulation and implementation of a model for Intramembranous Ossification is presented aiming to describe the complex process of bone tissue formation in tooth extraction sites. The model consists in a mathematical description of the mechanisms in which different types of cells interact, synthesize and degrade extra-cellular matrices under the influence of biochemical factors. Special attention is given to angiogenesis, oxygen-dependent effects and growth factor-induced apoptosis of fibroblasts. Furthermore, considering the depth-dependent vascularization of mandibular bone and its influence on bone healing, a functional description of the cell distribution on the severed periodontal ligament (PDL) is proposed. The developed model was implemented using the finite element method (FEM) and successfully validated by simulating an animal *in-vivo* experiment on dogs reported in the literature. A good fit between model outcome and experimental data was obtained with a mean absolute error of 3.04%. The mathematical framework presented here may represent an important tool for the design of future *in-vitro* and *in-vivo* tests, as well as a precedent for future *in-silico* studies on osseointegration and mechanobiology.

Keywords: Bone healing; Finite element method; Bioregulatory model; Hypoxia; Depth-dependent vascularization.

1. Introduction

A deep understanding of the complex biological and biochemical processes in bone's metabolism and the consequent capacity to predict its behavior has contributed to the development of novel medical techniques such as the localized administration of growth factors for assisted bone healing [1], the ultrasound-mediated bone regeneration [2], the careful and personalized selection of bone grafts, the development of scaffolds for regenerative medicine, among

many others that still have to be considered. Such an understanding has been traditionally obtained from *in-vitro* and *in-vivo* experimentation involving high costs at several levels. However, the latest advancements in computational modeling and computer power have boosted a new field of study that can shed light on such matters: *in-silico* testing.

It is possible to put forward mathematical models to describe the behavior of living tissues [3]. The *in silico* implementation of these models has a potential role in research and development of treatments, implants design and even in the prognosis of bone pathologies [4], significantly reducing the need for traditional testing techniques. Several mathematical models have been developed in order to understand the fundamentals of cell and tissue biology, and the behavior of biochemical factors in bone [5–15]. However, while most of the efforts have focused on studying regeneration and remodeling in long bones, to the authors' knowledge, few *in-silico* works emphasize

*Corresponding author
Carrera 30 45-03, Edificio 407, Oficina 213.

Email address: jpcorredorg@unal.edu.co (Jennifer Paola Corredor-Gómez)

Abbreviations:

BC: Blood clot

H-D: Hypoxia-dependent

IOM: Intramembranous ossification model

bone formation in the mandible, specifically regarding to intramembranous ossification (IO).

This paper presents the formulation of a mathematical model for predicting the spatiotemporal behavior of bone healing via IO. The model was validated by comparing its results with an *in-vivo* study of bone regeneration in tooth extraction sites. The proposed model builds on previous mathematical descriptions of fracture healing in long bones and incorporates modifications to account for the particular phenomena that take place in the mandibular bone. It also takes into account the findings by recent studies on the topic and introduces new biological and numerical considerations such as the growth factor-mediated apoptosis and a detailed description of the alveolar boundary conditions.

Our mathematical model can be used to predict the behavior of particular types of cells, the formation and degradation of important tissues and the action of growth factors during intramembranous bone healing, even in geometries that differ from the one used for validation. This makes possible to predict the events following a clinical intervention and to analyze some situations of compromised and assisted healing.

Due to the immense complexity of bone metabolism, and the lack of quantitative data and computational capacity [16], it is currently impossible to reproduce all the interacting biological, biochemical and mechanical processes by means of *in-silico* testing. This problem was tackled by making some simplifications and assumptions that helped the development of the current model. Furthermore, since a detailed histological examination of the alveolar bone regeneration in humans has many inherent difficulties, the validation of the model was performed by comparing the simulations outcome with an *in-vivo* study conducted in dogs as it is normally done.

2. Theoretical background: non-pathological bone healing

Bone tissue formation (also termed as ossification or osteogenesis) following injury is a complex process that involves the action of several cells and molecules. The different types of cells migrate, proliferate, differentiate, interact, synthesize and degrade extra-cellular matrices (ECM), proteins and enzymes under the influence of mechanical stimuli [17] and a variety of regulatory molecules. These molecules include insulin-like growth factors (IGFs), fibroblast growth factors (FGFs), platelet derived growth factors (PDGFs), transforming growth factors (TGFs), and bone morphogenetic proteins (BMPs), among others [18]. This process has been described by various authors as a recapitulation of the different embryological processes of bone formation: inflammation, repair and remodeling [19–21].

During bone formation, there are two distinct and interactive responses: endochondral and intramembranous ossification [17]. Endochondral ossification is characterized by chondrogenic growth factors and chondrocyte activity that allow the existence of cartilage; on the contrary, these aspects are absent in IO. Although the wound healing process in long bones (femur, tibia, ulna, etc.) has been clearly identified to occur via both responses [22–24], there has been an active discussion about which response takes place during bone formation in the mandible [25].

Both intramembranous and endochondral ossification have been reported to occur in the mandible during fetal development [26]. Nevertheless, many studies report absence of cartilage during bone regeneration, as will be seen later. De facto, three ossification centers operate in the mandible during fetal development: two predominant are intramembranous, whereas the third is an endochondral center within the Meckel's cartilage [25]. Endochondral ossification occurs only where the cartilage bar is near to the primary intramembranous centers; the process is transient and dimmed by the IO. After the cartilage is calcified, it is quickly invaded and surrounded by membrane bone and the endochondral osteogenic zones rapidly lose their identity [25].

One of the most common processes of bone healing in the mandible is the one that occurs inside an alveolus left by the extraction of teeth. It has been subject of multiple studies, both in animal and human specimens [27–32]. All authors describe the healing process in the extraction socket in the following sequence (note the absence of cartilage):

1. Formation and maturation of a blood clot (BC), which serves as initial construct for the healing process.
2. Replacement of the BC with a provisional matrix (PCT) synthesized by fibroblasts, which soon becomes the main construct for vascularization and cell migration.
3. Replacement of the PCT with newly formed woven bone.
4. Bone mineralization.
5. Bone remodeling.

At the time of tooth extraction, blood vessels are damaged resulting in bleeding and the consequent formation of a BC. The platelets contained in the blood release PDGF and TGF- β , together with vasoactive factors in a phenomenon called platelet degranulation [33], which concludes with vasoconstriction and the generation of a fibrin network [33]. The newly formed network serves as a scaffold for the migration of fibroblasts and mesenchymal stem cells (MSCs) that are attracted by both PDGF and TGF- β [34] and are originally immersed inside the bone marrow stroma [35]. BC is gradually degraded by the action of macrophages and plasmin (a protein contained in

plasma), contributing to the migration of MSCs and fibroblasts [36]. This initiates fibroplasia: the replacement of the blood clot with PCT and granulation tissue (GT), collagen-rich ECMs synthesized by fibroblasts which serve as a construct for angiogenesis [37]. While the fibrin clot forms within minutes [38], its degradation can take up to 7 days [27].

Angiogenesis is initiated from the severed blood vessel ends and is mainly mediated by the presence of vascular-endothelial growth factors (VEGFs) [39], which are endothelial cell mitogens and chemoattractants. These factors are produced in early stages of bone healing by cells in hypoxia conditions [40–42]. The resulting formation of vasculature is one of the primary driving mechanisms that facilitate the intramembranous bone formation [17, 43].

After the blood supply has been restored, a new phase begins. PCT is replaced by woven bone formed by osteoblasts, which differentiate from MSCs going through distinct intermediate stages (osteogenic cells) under the influence of several developmental signals. Among these are the Hedgehog, Wnt, Notch, BMP and FGF signaling pathways [44]. Osteogenic cells are chemotactically attracted by PDGF and TGF- β into the PCT [34] and afterwards mature osteoblasts synthesize a matrix consisting of 90% collagen proteins and 10% non-collagen proteins [19, 45]. This matrix is then mineralized and remodeled, completing the regeneration process.

3. Materials and Methods

3.1. Mathematical model for bone healing

The mathematical framework used in this study builds on the bioregulatory model developed by Geris *et al.* [13], which is based upon the work of Bailón-Plaza *et al.* [7] and Olsen *et al.* [46]. These models describe the biological phenomena that take place during fracture healing in long bones by modeling the concentration of several cell types in number of cells per unit volume (c_i), the density of different ECMs (m_j) and the concentration of various growth factors (g_k), both in mass per unit volume.

Later models by Peiffer *et al.* [14] and Carlier *et al.* [15, 47] were also reviewed and taken into account for the formulation of the intramembranous ossification model (IOM). Nevertheless, the discrete approximation of the blood vessels formation, which these latter models introduced, has not been adopted, since the results of the computational investigation by Geris *et al.* [13] show that the continuous approximation is accurate enough for the description of the angiogenesis influence on bone healing. The mathematical formulation consists in three different sets of equations.

For cell concentration:

$$\frac{\partial c_i}{\partial t} = \nabla \cdot \left[\underbrace{D_i \nabla c_i}_{\text{Diffusion}} - \underbrace{C_{i,CT} c_i \nabla g_i}_{\text{Chemotaxis}} - \underbrace{C_{i,HT} c_i \nabla m}_{\text{Haptotaxis}} \right] + \underbrace{A_i c_i [1 - \alpha_i c_i]}_{\text{Proliferation}} + \underbrace{\sum_{l \neq i} F_{li} c_l}_{\rightarrow \text{Differentiation}} - \underbrace{\sum_{n \neq i} F_{in} c_i}_{\text{Differentiation} \rightarrow} - \underbrace{d_i c_i}_{\text{Apoptosis}} \quad (1)$$

For ECM density:

$$\frac{\partial m_j}{\partial t} = \underbrace{P_{js} (1 - \kappa_j m_j) c_j}_{\text{Synthesis}} - \underbrace{Q_j m_j c_s \prod_r m_r}_{\text{Resorption}} \quad (2)$$

For growth factor concentration:

$$\frac{\partial g_k}{\partial t} = \underbrace{\nabla \cdot [D_{gk} \nabla g_k]}_{\text{Diffusion}} + \underbrace{\sum_p E_{gkp} c_p}_{\text{Production}} - \underbrace{\sum_t d_{gkt} g_k c_t}_{\text{Consumption}} - \underbrace{d_{gk} g_k}_{\text{Decay}} \quad (3)$$

The first term of equation 1 describes the migration of each cell type as a combination of diffusion, chemotaxis and haptotaxis. The diffusion term accounts for the random movement of cells, while the chemotactic and haptotactic terms represent the directed motion. The cell proliferation rate is considered proportional to the cell concentration up to a saturation value (α_i^{-1}). The \rightarrow Differentiation (differentiation from) term represents the differentiation into c_i from c_l , whereas the Differentiation \rightarrow (differentiation towards) term is associated with the decrease of c_i because of its differentiation into another cell type. The last term refers to cell apoptosis. The first term of equation 2 refers to the ECM synthesis by a specific type of cell (up to a maximum value κ_j^{-1}) and the second to its consumption, which can be associated with the formation of another ECM (m_r) or with the presence of certain type of cells (c_s). Equation 3 describes the changes in the concentration of the growth factor g_k as a result of its diffusion, its production by different cells (c_p), its natural decay and its consumption by some type of cell (c_t).

A schematic representation of the IOM is shown in Figure 1, which is mathematically described by the following system of 9 coupled partial differential equations (PDE):

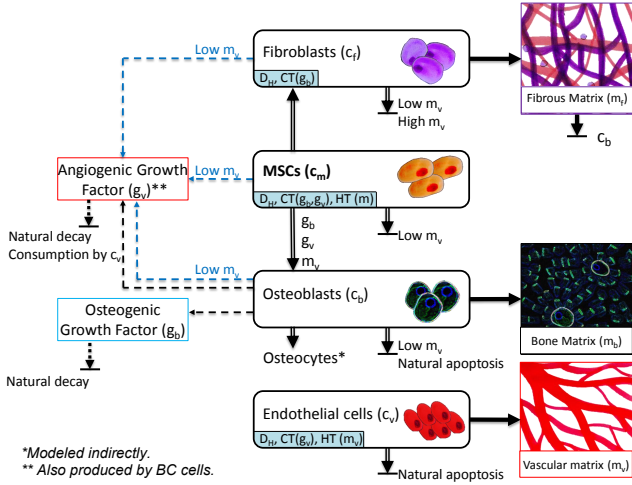


Figure 1: Graphical representation of the mathematical model. The inner blue boxes indicate the relevant modes of motility simulated for each cell: D_H stands for haptokinetic diffusion, CT for chemotaxis (chemo-attractant in brackets) and HT for haptotaxis (substrate in brackets). Dashed arrows indicate production of growth factors, double line arrows indicate differentiation and continuous line arrows indicate matrix synthesis. Blue dashed arrows refer to the H-D production of angiogenic growth factor (g_v). Arrows ending in a perpendicular line (\perp) indicate: decay or consumption of growth factors (dashed arrows); apoptosis (double arrows); tissue resorption or degradation (continuous arrows). *Inspired on the schematic representation by Geris et al. [13].*

$$\frac{\partial c_m}{\partial t} = \nabla \cdot [D_m \nabla c_m - C_{m,CT} c_m \nabla (g_b + g_v)] - \nabla \cdot [C_{m,HT} c_m \nabla m] + A_m c_m [1 - \alpha_m c_m] - F_{mb} c_m - F_{mf} c_m - d_m c_m \quad (4)$$

$$\frac{\partial c_f}{\partial t} = \nabla \cdot [D_f \nabla c_f - C_{f,CT} c_f \nabla g_b] + A_f c_f [1 - \alpha_f c_f] + F_{mf} c_m - d_f c_f \quad (5)$$

$$\frac{\partial c_b}{\partial t} = A_b c_b [1 - \alpha_b c_b] + F_{mb} c_m - F_{bo} c_b - d_b c_b \quad (6)$$

$$\frac{\partial c_v}{\partial t} = \nabla \cdot [D_v \nabla c_v - C_{v,CT} c_v \nabla g_v - C_{v,HT} c_v \nabla m_v] + A_v c_v [1 - \alpha_v c_v] - d_v c_v \quad (7)$$

$$\frac{\partial m_f}{\partial t} = P_{fs} (1 - \kappa_f m_f) c_f - Q_f m_f c_b \quad (8)$$

$$\frac{\partial m_b}{\partial t} = P_{bs} (1 - \kappa_b m_b) c_b \quad (9)$$

$$\frac{\partial m_v}{\partial t} = P_{vs} (1 - \kappa_v m_v) c_v \quad (10)$$

$$\frac{\partial g_b}{\partial t} = \nabla \cdot [D_{gb} \nabla g_b] + E_{gbb} c_b - d_{gb} g_b \quad (11)$$

$$\frac{\partial g_v}{\partial t} = \nabla \cdot [D_{gv} \nabla g_v] + E_{clot} m_f + E_{gvm} c_m + E_{gvf} c_f + E_{gvb} c_b - g_v (d_{gv} + d_{gvc} c_v) \quad (12)$$

Where the four types of cells are MSCs (c_m), fibroblasts (c_f), osteoblasts (c_b) and endothelial cells (c_v); the three different ECMs are fibrous matrix (m_f), bone matrix (m_b) and vascular matrix (m_v); and the two different generic growth factors are osteogenic growth factor (g_b)

Table 1: Description of variables for each biological set.

Biological set	Variable	Definition
Cells	c_m	Mesenchymal Stem Cells
	c_f	Fibroblasts
	c_b	Osteoblast
	c_v	Endothelial Cells
Tissues (ECMs)	m_f	Fibrous matrix
	m_b	Bone matrix
	m_v	Vascular matrix
Growth factors	g_b	Osteogenic growth factor
	g_v	Vascular growth factor

and angiogenic growth factor (g_v) (Table 1).

Since the ossification response that takes place in tooth extraction sites is intramembranous, the equations describing chondrocyte concentration, density of cartilaginous ECM and concentration of chondrogenic growth factor were removed from the original set of equations. As in previously reviewed models by Geris *et al.* [8, 13], Peiffer *et al.* [14] and Carlier *et al.* [15, 47], the fibrous matrix corresponds to BC, GT and PCT. Likewise c_m represent not only MSCs but also intermediate stages of differentiation. Additional changes to the original mathematical model proposed by Geris *et al.* [13] will be discussed later in this article.

Note that chemotaxis of osteoblasts has been ignored here because it is negligible, as reported by Peiffer *et al.* [14]. It is also noteworthy that in all the reviewed models, both the fibroblast apoptosis and the fibrous matrix resorption are dependent on the appearance of cartilage (either directly or indirectly, due to the hypertrophy of the chondrocytes). However, this dependency has not been adopted in the present work, since there is no chondrogenesis. This aspect is discussed more extensively in section 4. As proposed by Carlier *et al.* [47], all but the endothelial cells produce angiogenic growth factor in hypoxic conditions. It is important to mention that all PDEs must be non-dimensionalized. The non-dimensional variables will be denoted with a tilde (see Appendix A).

Further modifications to the original model of 2008 were made for three main reasons. First, so that the FEM implementation be numerically more stable. Second, in order to adopt important modifications made in more recent publications [14, 15, 47]; and finally, to consider additional biological phenomena reported in the literature.

The conducted procedure to determine the parameters' values used in the model was made through the following steps:

1. Parameters from previous models were adopted.
2. An extensive literature review was made in order to update and verify the parameters' values. This data was found in different *in-vivo* and *in-vitro* studies, leading to a modification of some of the previously

adopted parameters and also to an incorporation of new parameters.

3. The adopted parameters were non-dimensionalized. (See [Appendix A](#) for detail).
4. Since some of the parameters' values were not reported in the literature and *in-vivo* or *in-vitro* experiments could not be performed, an exhaustive sensitivity analysis was conducted in the interest of estimate the numerical values.

In the following subsections, we present the most important modifications incorporated into the IOM.

3.1.1. Modifications to improve the numerical stability

In the FEM implementation, the small magnitudes of \tilde{m}_v and \tilde{c}_v , together with the larger values of the other variables that result from the approach developed by Geris *et al.* [\[13\]](#), led to inconveniences regarding the condition number of the system matrices ($\tilde{c}_v = O(10^{-4})$, $\tilde{m}_v = O(10^{-7})$, $\tilde{g}_b = O(10)$, etc.). This problem was overcome by changing the non-dimensionalization, *i.e.* choosing the characteristic concentration of endothelial cells as $c_{v,0} = 100$ cells/ml (shown in more detail in [Appendix A](#)). This leads to a boundary value of $\tilde{c}_{v,bc} = 1$ in the original long bone non-union model.

Taking into account that the resulting $\tilde{c}_{v,bc}$ is the same as in the model of Olsen *et al.* [\[46\]](#), $m_{v,0}$ was also changed in order to adopt their approximation for the vascular matrix synthesis rate by endothelial cells (\tilde{P}_{vs}), as well as the ECM saturation value ($m_{v,max} = \kappa_v^{-1}$). Due to the new non-dimensionalization for the vascular matrix and the lack of quantitative data in the literature, $C_{v,HT}$ was redefined in the continuous model by adopting the $D_v/C_{v,HT}$ ratio in accordance with the parameters reported by Olsen.

The value of $\tilde{\alpha}_v$ that was derived from the data of Geris *et al.* [\[13\]](#) resulted to be too small in comparison with the value of other variables, as it allowed the growth of the endothelial cell population up to $\tilde{c}_v \approx O(10^3)$ in some points inside the domain (data not shown). In order to obtain homogeneous order of magnitude of the non-dimensionalized variables, the saturation value for the proliferation of endothelial cells was set to $\tilde{\alpha}_v = 1$, which is consistent with the value reported by Olsen *et al.* [\[46\]](#).

Another form of numerical instability like oscillatory behavior could occur due to the convective nature of the chemotactic and haptotactic terms. It imposes a problem for the stability of the Petrov-Galerkin discrete solutions. These instabilities were dealt with by incorporating the stabilization procedure for chemotaxis problems proposed by Strehl *et al.* [\[48, 49\]](#).

3.1.2. Incorporation of vascularization-dependent effects

Carlier *et al.* [\[47\]](#) made an exhaustive literature review about the influence of oxygen tension in most of the

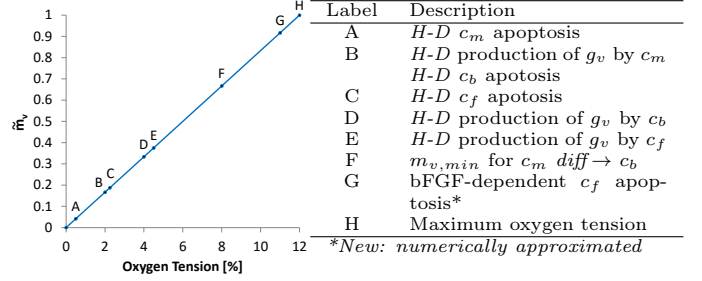


Figure 2: Assumed functional relationship between oxygen tension and \tilde{m}_v . The processes are listed in the table according to the data reported by Carlier *et al.* [\[47\]](#)

biological processes that occur during bone fracture healing. Their approach was adopted in the present work and adapted to the continuous angiogenesis under two assumptions: first, that the oxygen tension in each part of the domain is proportional to the vascularization (\tilde{m}_v); and second, that the maximum oxygen tension during bone healing (taken as 12% as reported by Brighton *et al.* [\[50\]](#)) corresponds to the maximum value of \tilde{m}_v . The following oxygen-dependent processes were considered (see Figure 2):

1. Apoptosis due to hypoxia (labels A, B and C) [\[51, 52\]](#).
2. H-D production of angiogenic growth factor (labels B, D and E) [\[47, 53\]](#).
3. Minimum oxygen tension for intramembranous ossification (label F) [\[43\]](#), taken as that required for osteoblast differentiation from MSCs [\[47\]](#).

In a recent study, Akasaka *et al.* [\[54\]](#) found that the mechanisms underlying fibroblast apoptosis during wound healing are closely related with the appearance of certain growth factors. They reported that the basic fibroblast growth factor bFGF (or FGF-2, as it is also known) promotes the apoptosis of injured tissue-derived fibroblasts that were previously treated with transforming growth factor TGF- β 1. It is well known that endothelial cells express bFGF to produce autocrine effects [\[55–57\]](#) and that TGF- β 1 is produced by platelets during the initial clot formation [\[58\]](#) [\[59\]](#). Hence, an increase in fibroblast apoptosis can be expected at high vascularizations.

Taking into account the reasons mentioned above, the current analysis introduces fibroblast apoptosis as an additional process that depends \tilde{m}_v . Because of the lack of available quantitative experimental data in the literature, the fibroblast apoptosis term was firstly adopted in the same way as Carlier *et al.* described the apoptosis of chondrocytes due to high oxygen tensions [\[47\]](#). Nevertheless, the magnitude of the apoptosis rate was changed numerically, in order to reproduce the experimental data of Cardaropoli [\[27\]](#) (see section 4 and label G in Figure 2).

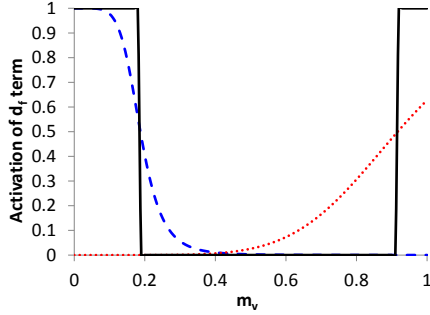


Figure 3: Comparison between the activation functions for H-D fibroblast apoptosis using a 6th order Hill function (—), bFGF-dependent fibroblast apoptosis using a 6th order Hill function (···) and both thresholds modeled with a Heaviside constant function (—)

3.1.3. Thresholding models

Previous works used sixth-order Hill functions to model thresholds [7, 13, 14, 47]. In the case of fibroblast apoptosis, the biological phenomena discussed above is expressed mathematically by an equation of the form:

$$\tilde{d}_f = \frac{\tilde{d}_{f,hyp} \tilde{H}_{hyp}^6}{\tilde{H}_{f,hyp}^6 + \tilde{m}_v^6} + \frac{\tilde{d}_{f,bFGF} \tilde{m}_v^6}{\tilde{H}_{f,bFGF}^6 + \tilde{m}_v^6} \quad (13)$$

Where $\tilde{H}_{f,hyp}$ is the threshold for H-D apoptosis, \tilde{H}_{bFGF} is the threshold for the bFGF-dependent apoptosis, $\tilde{d}_{f,hyp}$ and $\tilde{d}_{f,bFGF}$ are the corresponding apoptosis rates. This kind of functions are appropriate for modeling thresholds when the variables analyzed are small (as in the reviewed publications). However, when the threshold value is big, the Hill function becomes wide. As can be seen in Figure 3, the activation function for the bFGF-dependent apoptosis (red dotted line) is much wider than the activation function for the H-D apoptosis (blue dashed line). If Hill functions were used, fibroblasts would undergo apoptosis for almost any condition of vascularization. Similarly, the oxygen-dependent differentiation of osteoblasts from MSCs exhibits a too smooth behavior. As a consequence of this analysis, all thresholds in the present work are modeled with Heaviside functions (black continuous line), which at the same time reduces computational cost. Consequently, equation 13 is replaced by:

$$\tilde{d}_f = \begin{cases} \tilde{d}_{f,hyp} & \text{if } 0 \leq \tilde{m}_v < \tilde{H}_{hyp} \\ 0 & \text{if } \tilde{H}_{hyp} \leq \tilde{m}_v < \tilde{H}_{bFGF} \\ \tilde{d}_{f,bFGF} & \text{if } \tilde{H}_{bFGF} \leq \tilde{m}_v \end{cases} \quad (14)$$

As can be inferred, the parameters in equations 4-12 can be constant or dependent on the modeled variables. Table 2 provides a summary of the non-constant parameters and illustrates their functional behavior. It is important to point out that the bell-shaped curves have different mathematical descriptions depending on the process being modeled (for more information about the mathematical background see [7, 13, 46]). The numerical parameters are enunciated in Appendix A.

3.1.4. Clot-induced angiogenesis

Despite of the fact that BC was not considered as an individual matrix, the effect of this temporal tissue on recruiting newly formed vasculature is of outmost importance, and hence included in the model. To this end, a thresholding model was applied for the production of \tilde{g}_v by BC (see second term in eq. 12). This production rate was deemed constant for low values of m_v and zero for high values of m_v .

3.1.5. Additional considerations

As in [14, 15, 47], \tilde{g}_v production by osteoblasts was modeled to be high for low angiogenic growth factor concentrations. These recent studies excluded the original requirement of g_v for the osteoblast differentiation [13]. However, this term was maintained in the present work because of its observed influence in the simulation results and its reported importance [60, 61]. Thus, four factors are required for osteoblast differentiation: c_m , m_v , g_v and g_b .

Finally, the differentiation parameters used by Carlier *et al.* [47] were adopted. These parameters are listed in Table A.4. Remark that all the thresholds were adapted to the new description of vascularization-dependent effects.

Unless it is explicitly indicated in the text, the parameters for equations 1-3 were defined exactly as by Geris *et al.* [13]. In this sense, the haptokinetic behavior of the diffusivity parameters for cells (D_i in equation 1) is modeled as a bell-shaped curve with the following expression:

$$D_i = \frac{D_{hi}m}{K_{hi}^2 + m^2} \quad (15)$$

Following the same methodology as Geris *et al.* [13], the parameter D_{hv} was adjusted, so that the maximum value of the bell-shaped function corresponds to the diffusivity value reported by Rupnick [62] in their *in-vitro* experiments. Due to the lack of exact quantitative information in the literature, the value of K_{hv} reported by Geris was adopted. The result of the described methodology yields:

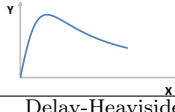
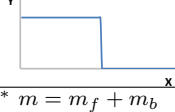
$$D_{hv} = 1.41696 \times 10^{-5} \frac{g \times mm^2}{day} \quad (16)$$

Similarly, the fibroblast diffusivity was taken from the numerical study by Olsen *et al.* [63]. Remark that all parameters were adimensionalized as described in Appendix A.

3.2. Tooth extraction model

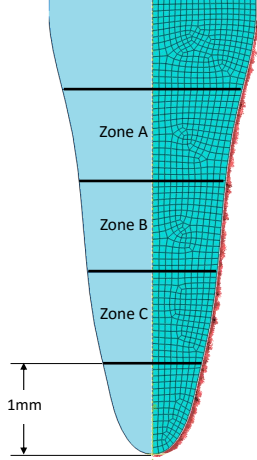
The healing of an extraction socket following tooth removal in dogs [27] was simulated. In this experimental model, the distal root of the fourth premolar of nine mongrel dogs (12 months old and of about 10 kg) was extracted, damaging the bone tissue structure and triggering a healing process. The dogs were sacrificed at several time points after the extraction and the volume occupied by

Table 2: Behavior of non-constant parameters of equations 4-12 depending on simulated variables.

Behavior	Phenomenon	Y	X
Bell-shaped			
	Haptokinetic diffusion Chemotaxis Haptotaxis Cellular proliferation	D_i ($i = m, v$) $C_{i,CT}$ ($i = m, f, v$) $C_{m,HT}$ A_i	m^* g_k ($k = b + v, b, v$) m^* m^*
	bFGF-dependent apoptosis Osteoblast differentiation	d_f F_{mb}	m_v m_v
	H-D g_v production H-D apoptosis g_v production by osteoblasts g_v production by BC	E_{gvi} d_i ($i = m, f, b$) E_{gvb} E_{clot}	m_v m_v g_v m_v
$* m = m_f + m_b$			



(a) Histological examination at first day after tooth extraction [27].



(b) Modeled geometry and mesh. Injured border for boundary conditions shown in red.

Figure 4: Geometry for the simulations.

different types of tissues (BC, GT, PCT, woven bone and mineralized bone) was determined by histomorphometric examination.

The geometry used for the simulations was obtained from a histological examination of the extraction zone taken one day after tooth extraction (Figure 4(a)). The dimensions of the socket and the distribution of the histological sections were derived from the description made by Cardaropoli *et al.* [27], resulting in the representation in Figure 4(b), which is 5 mm deep and has a coronal diameter of 2.26 mm. Each histological zone is 1 mm high. These dimensions are coherent with the ones reported by Araújo *et al.* in a dimensional study in mongrel dogs of the same age and size [28].

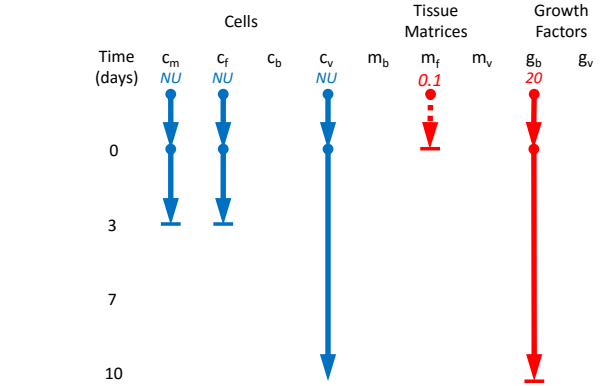


Figure 5: Model conditions: graphical representation. Continuous and dashed lines represents boundary and domain conditions respectively. Blue lines indicate non-uniform (NU) conditions, which depend on wound depth (Figure 6), while red lines are defined homogeneously. Arrows ending in a horizontal line mean that the condition is released at that precise moment.

3.3. Boundary and initial conditions

Figure 5 shows all boundary and initial conditions prescribed. As in previous works [13–15, 47], no-flux boundary conditions (von Neumann) were prescribed on all borders, while Dirichlet boundary conditions were imposed for certain variables on the injured border (Figure 4(b)) for stipulated timespans. Cardaropoli *et al.* found large numbers of MSCs, fibers and dilated vascular units on the severed PDL[27]. Therefore, c_m , c_f and c_v were supposed to originate from the surrounding borders. The boundary condition for osteoblasts used by Geris *et al.* [13] was not set (as in [14] onward).

McCulloch *et al.* [64, 65] studied the communication of endosteal bone with the PDL in mouse alveoli and indicated its direct influence on cell populations. They showed that the percentage of vascular channels (PVC) which com-

municate with bone marrow varies depending on the depth, being the inner bone richer in vascularization than the outer bone. A regression analysis yielded that the experimental data reported by McCulloch can be approximated using an exponential regression with a high correlation coefficient ($R^2 = 0.995$). Therefore, we have prescribed the density of MSCs, fibroblasts and endothelial cells in the border adopting the same exponential distribution. The corresponding apical cell densities on the boundary were set at $\tilde{c}_{m,bc} = \tilde{c}_{f,bc} = 3.76 \times 10^{-3}$ and $\tilde{c}_{v,bc} = 0.188$. These values were calculated taking into account the following:

- The PVC ratio between alveolar cortex and femoral neck reported by Kingsmill *et al.* [66] and Young *et al.* [67].
- The boundary conditions established by Geris *et al.* [13] and Olsen *et al.* [46].

Moreover, the calculated PVC ratio between the alveolar most coronal and most apical sections is 5.77×10^{-2} [64]. Thereupon, the value for MSCs and fibroblasts on the coronal region was set at $\tilde{c}_{m,bc} = \tilde{c}_{f,bc} = 2.1687 \times 10^{-4}$ and endothelial cells at $\tilde{c}_{v,bc} = 0.0108$. Figure 6 shows the non-dimensional density of cells prescribed along the injury border. In spite of the presence of endothelial cells on the injured bone end, \tilde{m}_v was not prescribed as a boundary condition due to the tissue impairment caused during the extraction procedure.

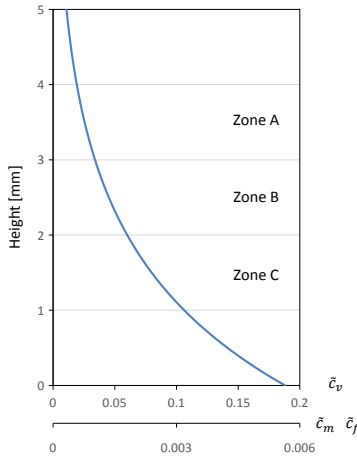


Figure 6: Boundary value of MSC, fibroblast and endothelial cell density ($\tilde{c}_{m,bc}$, $\tilde{c}_{f,bc}$ and $\tilde{c}_{v,bc}$ respectively) versus depth of injury. The cell distribution was adjusted using the same functional form obtained by regression from the experimental data reported by McCulloch *et al.* [64, 65] and taking into account the boundary conditions proposed by Geris *et al.* [13] and the PVC ratio from Kingsmill [66].

Geris *et al.* set $\tilde{g}_{b,bc} = 20$ homogeneously on the injured cortical bone border during the first 10 days [13]. Since the bundle bone (which is mostly cortical) was exposed during the removal of the premolar, this boundary

condition was adopted.

The initial condition for the fibrous matrix was defined as $\tilde{m}_{f,0} = 0.1$ in the whole domain [13] (representing only BC at this time point). A sensitivity analysis showed that the initial condition for \tilde{g}_v is negligible for the case study.

3.4. Numerical implementation

The implementation of the reaction-diffusion-taxis coupled PDE system was achieved by means of FEM. Equations 4-12 were discretized using the Petrov-Galerkin approach and the code for assembling the system matrices (mass, stiffness and flux) was written in Fortran 90. In order to ensure mass conservation and improve numerical performance, a generalized flux-corrected transport algorithm (lumping method) proposed by Strehl *et al.* [48, 49] was used. Since all analyzed variables must be positive, non-negativity was guaranteed by both lumping and active adaptation of time increments.

Half of the modeled geometry was simulated taking into account axisymmetrical behavior. The mesh was made up of 907 quadrilateral elements with bi-linear shape functions (Figure 4(b)).

4. Results and discussion

Bars in Figure 7 show the histologically measured tissue fractions [27] for fibrous tissue and bone in histological zones A, B and C at days 1, 3, 7, 14, 30 and 60 after tooth extraction. The computationally predicted tissue fractions are illustrated as follows: IOM (red continuous line), IOM without bFGF-dependent fibroblast apoptosis (green dashed line) and IOM using different boundary conditions (blue dotted line and black dash-dot line). For the intermediate states (days 14 and 30) the error bars indicate the standard deviation of the experimental data, whereas at days 1, 3 and 7 only fibrous tissue was observed and at day 60 only bone tissue was reported [27].

The predicted tissue fractions in each node were obtained with the following mathematical expression:

$$\chi_j = \frac{\tilde{m}_j}{\tilde{m}_f + \tilde{m}_b} \quad (17)$$

Afterwards, the average tissue fraction for all the nodes located in each histological zone was computed in every time increment, in order to generate the curves that are shown in Figure 7. The mean absolute error for the IOM is 3.04%, for the green dashed line 5.18%, for the blue dotted line 4.40% and for the black line 13.1%.

4.1. Intramembranous ossification model (IOM)

The ossification process starts shortly after day 7, which is consistent with the data of Cardaropoli *et al.* [27]. The

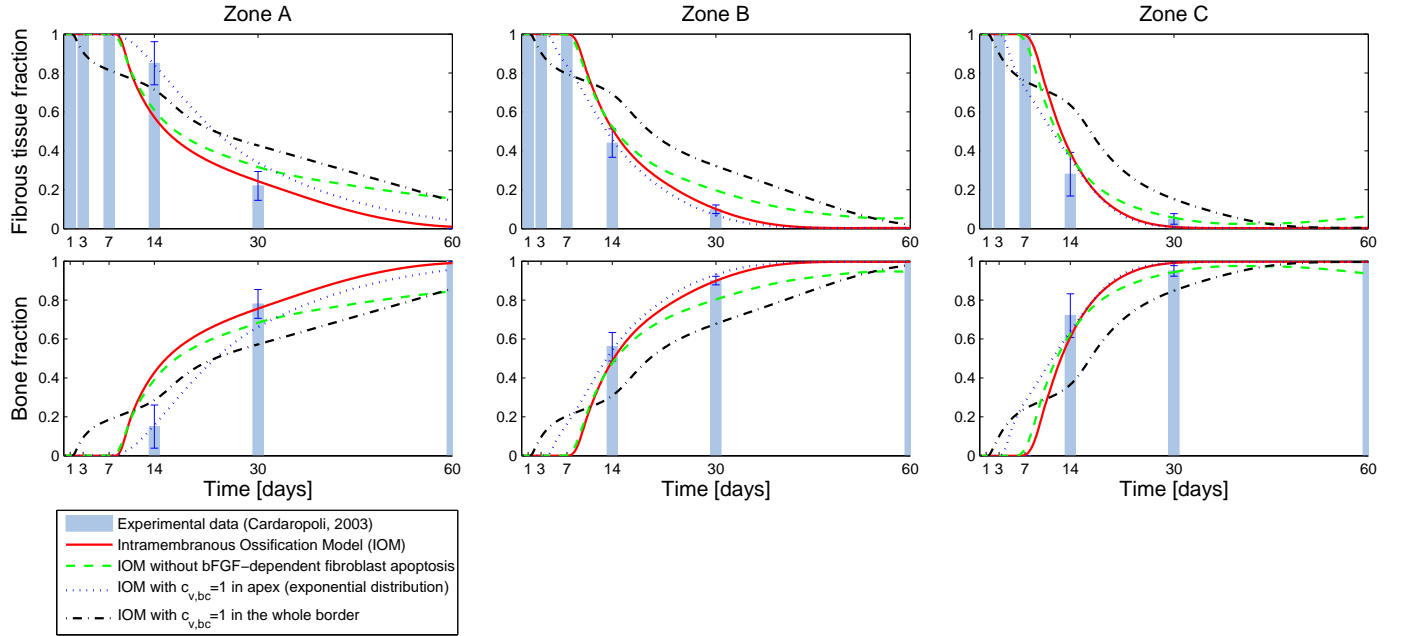


Figure 7: Bone and fibrous tissue fractions in alveolus. The bars (average \pm standard deviation) represent the histologically measured values at 1, 3, 7, 14, 30 and 60 days after tooth extraction (see section 3.2). The curves are the tissue fractions predicted by the Intramembranous Ossification Model (IOM) and its modifications.

ossification rate increases suddenly and then slowly decreases (see also Figure 11). Around day 14, angiogenic factors (\tilde{g}_v) are depleted and the osteoblast differentiation stops. Consequently, the population of osteoblasts can only increase by means of proliferation. This and the synthesis saturation expressed in equation 9 cause a deceleration in bone formation.

Note that the ossification is triggered first in *Zone C*, then in *Zone B* and lastly in *Zone A* and that the bone formation rate is slower in the upper zones. This is a consequence of the higher concentration of \tilde{c}_m and \tilde{m}_v (produced by the prescribed boundary conditions), and the geometrical characteristics of the different zones. Since the apical regions are smaller, the initial ossification on the surrounding borders (Figure 8) results in an accentuated increase in bone fraction.

The spatio-temporal distribution of tissues obtained in the simulations is shown in Figure 8 and the contours for cells and growth factors are shown in Figures 9 and 10, respectively. It can be seen that fibrous tissue is degraded as bone is formed from the injured borders inwards and bottom up, in accordance with the investigation of Cardaropoli *et al.* [27].

4.1.1. Days 0-14

The gradient of cells described by the exponential definition on the boundary induces bottom up and inward diffusion. MSCs and fibroblasts invade the socket area from the injured bone ends secreting angiogenic growth

factors due to hypoxia, which along with the \tilde{g}_v produced by BC fills up the entire domain. Meanwhile, the autocrine and paracrine role of angiogenic growth factors expressed by the MSCs promotes clustering in the center of the socket. Further concentration of MSCs is seen on the wound edge as a result of the chemotactic response to osteogenic growth factors.

During the early stages of wound healing, the big amounts of the produced angiogenic growth factors degrade rapidly and are consumed by the endothelial cells during angiogenesis. At day 7, \tilde{g}_v is almost completely consumed and some clusters of endothelial cells can be observed as a vascularization-forming traveling wave advances through the domain. Remark that the wave comprises two advancing peaks that propagate through the socket, whose maximum values are slightly greater than $\tilde{c}_v = 1$ (saturation value for proliferation) in zones where chemotactic and haptotactic effects are significant.

As soon as the boundary condition for \tilde{g}_b is released, the border MSCs begin to migrate triggering the ossification front advance. Meanwhile, the central cluster mainly differentiates into fibroblasts favored by the absence of g_b . At the 14th day, fibrous tissue synthesized by the cluster of fibroblasts is observed in the wound center as well as in two isolated points near the border of the apical and coronal zones. This latter formation can be explained by both the differentiation of MSCs into fibroblasts and a previous chemotactic migration of c_f towards high \tilde{g}_b spots, which are favored by the absence of fibroblast apoptosis (the vas-

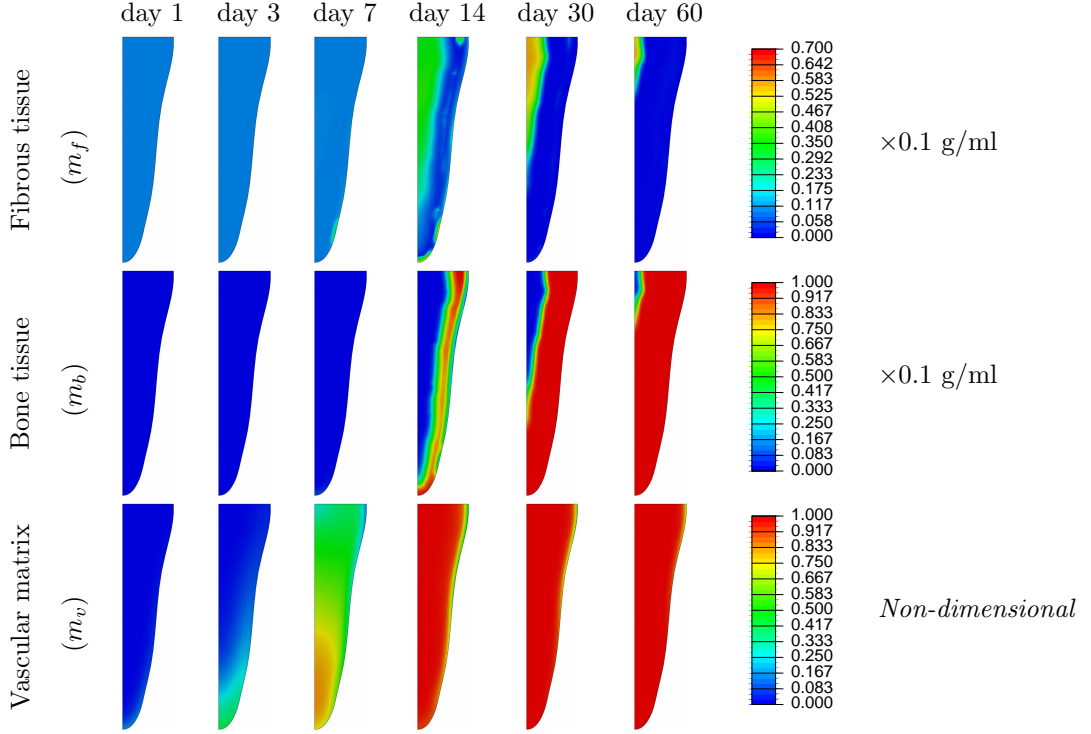


Figure 8: Spatiotemporal distribution of ECMs: Fibrous tissue (m_f), bone (m_b) and vascular tissue (m_v).

cularization is neither too high nor too low to induce it).

4.1.2. Days 14-30

Between days 14 and 30, vascular ECM is formed from the root canal upwards, filling almost completely the whole extraction socket by day 14th. This causes bFGF-dependent fibroblast apoptosis to become dominant, which, together with the presence of osteoblasts, leads to a rapid resorption of fibrous tissue. At this time, the ossification front advances over the domain towards the center of the injury from the apical to the coronal zones. As can be seen in Figures 9 and 10, the osteogenic growth factor distribution is similar to the osteoblasts', which illustrates the autocrine and paracrine behavior.

The decreasing population of fibroblasts clustered in the central coronal area achieves to densify the fibrous matrix in this area. When the formation of blood vessels is concluded, the distribution of endothelial cells accommodates to resemble the boundary condition.

4.1.3. Days 30-60

Between days 30 and 60, the ossification front advances continuously as expected. The deceased fibroblasts on the central coronal zone left behind a densified fibrous tissue in that area. At day 60, the bone tissue is not yet formed at the coronal center of the socket, as can be observed in the histologies reported by Cardaropoli [27]. At the end of the

simulation, MSCs have proliferated through the whole domain populating the newly formed bone marrow, making possible the subsequent processes, such as bone remodeling and eventually wound healing.

Figure 11 illustrates bone formation rates (BFR) for the three alveolar zones. After the ossification process is triggered at around day 7, the initial BFR is similar for all zones. The peak BFRs are 12.30%/day, 10.86%/day and 12.14%/day for Zone A, B and C, respectively and occur around day 10.

4.2. Modifications to the IOM

The green dashed line of Figure 7 depicts that the absence of bFGF-dependent fibroblast apoptosis produces a late and unexpected densification of the fibrous tissue in all zones, leading to an increase in fibrous matrix proportion in comparison with bone tissue. Without the apoptosis term, fibroblasts continue to proliferate and create excessive ECM, as can be seen in Zone C, where a growth trend of fibrous tissue is shown.

The blue dotted line in Figure 7 shows the IOM predictions when the boundary condition is changed. The exponential function for cell density on the injured border (section 3.3) was used, but the boundary values for c_m , c_f and c_v were not scaled to account for the difference in vascularization between long bones and the mandible.

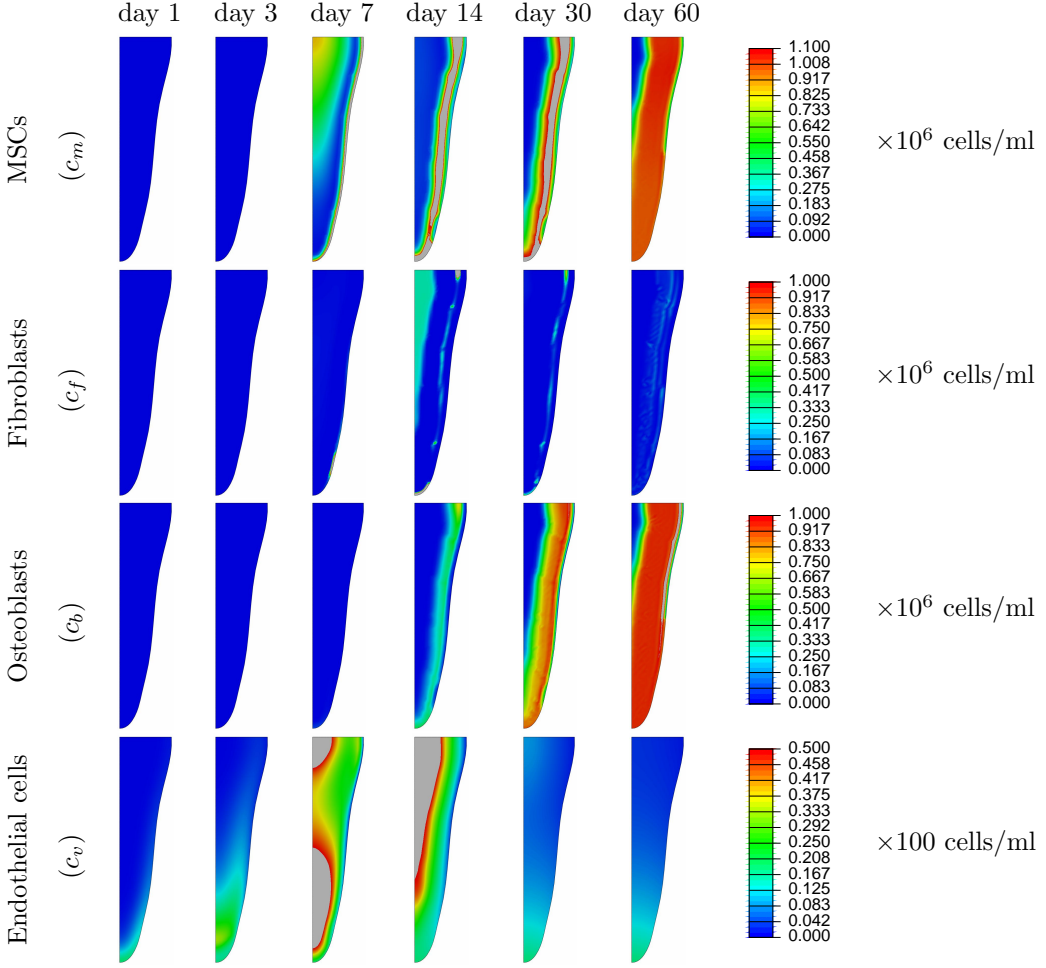


Figure 9: Spatiotemporal distribution of cells: MSCs (c_m), fibroblasts (c_f), osteoblasts (c_b) and endothelial cells (c_v).

This approach seems to fit better the histological observations in *Zone A*, but it is detrimental for the prediction in *Zones B* and *C*. Since there are many endothelial cells on the boundary, vascularization is formed faster than in the IOM. In *Zone A*, endothelial cells reach the spots with high concentration of g_v and consume it before there is enough g_b to allow osteoblast differentiation.

In *Zones B* and *C*, bone formation and the correspondent fibrous tissue degradation are very similar to the IOM from day 14 onward. However, bone formation begins much earlier. This phenomenon responds to the fact that three of the four required conditions for osteoblast differentiation are magnified: the amount of MSCs on the apical region, the production of angiogenic growth factor and the formation of vascular ECM. Approximately at day 14, endothelial cells regulate the concentration of angiogenic growth factors on the apical region by consuming them. By doing so, osteoblast differentiation slows down, as in the IOM.

For the black dash-dot line in Figure 7, the boundary

condition for c_m , c_f and c_v was uniform and unscaled. The early bone formation that was observed in the blue dotted line is more accentuated and also present in *Zone A*. Then, the BFR slows down, producing a pronounced mismatch with the experimental data. The importance of an accurate description of the boundary values becomes clear.

4.3. Limitations of the IOM

As can be observed in Figure 7, there is a mismatch with the experimental data at day 14 in *Zone A*. These dissimilarities may be a consequence of not simulating the stages of clot formation and resorption. Even though the blood clot, the provisional matrix and the granulation tissue are all fibrous tissues, they are formed and degraded at different time points of the bone formation process. Experimental studies [27, 31] show that the big primary BC needs to be degraded in order to leave space for PCT and GT, which serve as scaffolds for cell migration and consequent vascularization [68]. Since there would be a greater volume of BC to resorb in *Zone A*, the incorporation of BC dynamics might result in a delayed bone formation

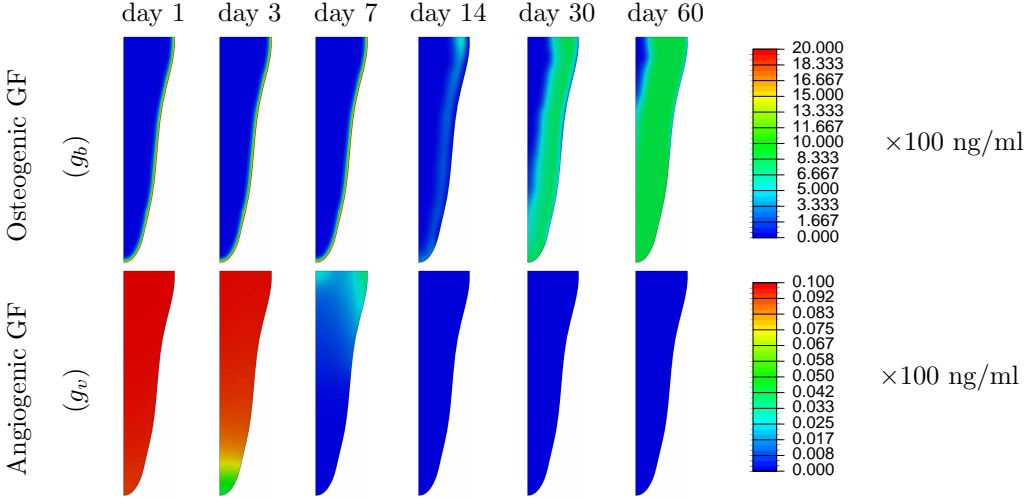


Figure 10: Spatiotemporal distribution of growth factors: osteogenic growth factor (g_b) and angiogenic growth factor (g_v).

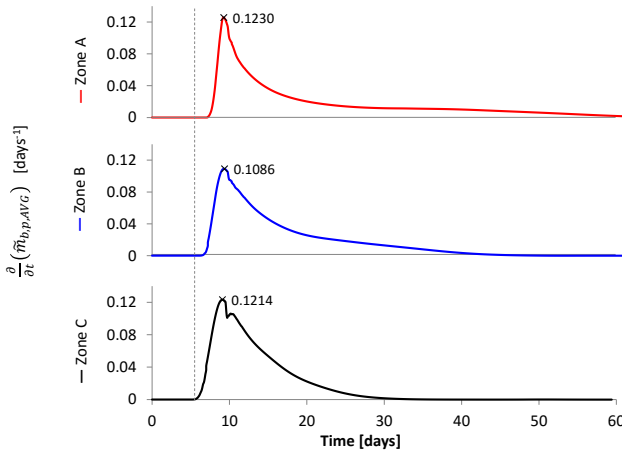


Figure 11: Derivatives of the averaged tissue fractions.

and will be the subject of future work.

The discrepancy in tissue fractions in *Zone C* at day 30 may be explained by the high osteoblast density over the areas of recently formed bone (Figure 9). In order to avoid this effect, a rigorous review of the mechanisms that underlie the regulation of the osteoblast population via apoptosis and osteocyte differentiation at high woven bone densities ought to be made. Another possible explanation for the disparities is that the trans-differentiation of fibroblasts into osteoblasts during the intramembranous ossification [69, 70] was not considered.

In the IOM, the saturation terms for cell proliferation (equations 4-7) are only dependent on each cell population. However, due to the existent competition for space and nutrients, saturation limits for cell proliferation de-

pend not only on the population of a given cell type but also on that of other kinds of cells. Similarly, the synthesis saturation for each ECM (equations 8-10) considers only the specific tissue maximum density. A revision of the saturation mathematical terms will be addressed in future studies.

Since the processes that take place in the surrounding tissue were not simulated, their effect on the bone formation inside the alveolus had to be captured with boundary conditions (as in [13-15, 47]). However, the surrounding bone marrow and cortical bone are influenced by both mechanical and biological processes. In point of fact, Araújo *et al.* [28] illustrates how the alveolar ridge dimensions are altered after the tooth extraction on 10 kg mongrel dogs. In the absence of a tooth, bone resorption caused by low mechanical loading can be observed and a retraction of the neighboring bone marrow to more apical zones may be expected. As seen in section 3.3, this would modify the injured PDL cell populations, *i.e.*, the boundary conditions should not be constant but time dependent.

The resorption and elimination of fibrous tissue are a consequence of both the metalloproteinases produced by osteoblasts and the action of macrophages [71], which enter the domain along with the osteoblasts. However, due to the lack of quantitative data, fibrous matrix degradation was modeled as proportional to the osteoblast concentration (equation 8). By doing so, bone healing was supposed to occur as in a healthy individual. For some pathologies, the action of the macrophages may have to be modeled separately. Further research is needed in order to describe in more depth the processes that underlie fibrous tissue degradation.

Due to the lack of information about the 3D character-

istics of the alveoli, the simulation domain was modeled from a 2D-histology and supposed to have axisymmetric behavior. This could have introduced some error in the outcome. The mathematical model and the computational implementation presented in this article could also be implemented in geometries obtained from 3D medical imaging tools (such as CT-scan or MRI). Nonetheless, the computational cost would be much higher.

Fluctuations in oxygen tension due to consumption by cells may occur. Since oxygen tension was not directly simulated these fluctuations cannot be observed in the present study. A possible manner to overcome this issue is to use an approach like the one shown by Carlier *et al.* [47].

Future models must take into consideration the individual action of the different growth factors in order to better depict the biological phenomena. For instance, even though it has been reported that bFGF acts as an angiogenic growth factor (it has autocrine and paracrine effects on endothelial cells [55, 56]), the new fibroblast apoptosis term was not implemented as dependent on \tilde{g}_v . The reason is that fibroblast apoptosis would be incorrectly induced in early stages of the bone healing process, since all the cells produce VEGF (another angiogenic growth factor) in hypoxia conditions. Ergo, a more precise model would differentiate between VEGF and bFGF. Similar behaviors can be identified for the BMPs (1–8), GDFs (1, 5, 8, and 10), and TGF β 1, which contribute to both endochondral and intramembranous ossification [17].

In the present approach, as in many of the cited works, mesenchymal stem cell differentiation into other types of cells is modeled as a reaction term. This assumes that the differentiation takes place immediately. However, cell differentiation is a gradual process, in which cells pass through a series of intermediate stages by expressing different phenotypes under the influence of both mechanical and biochemical signals[44]. A way of dealing with this phenomenon could be keeping track of the gradual change of cell phenotype (as in the work by Prokharau *et al.* [72]). Another solution to the problem could be to explicitly include some of the intermediate stages of differentiation in the model. These approaches will be addressed in future studies.

5. Conclusions

- A new mathematical model for intramembranous ossification was developed and validated with experimental data taken from the literature [27]. It is, to the best of our knowledge, the first model that describes intramembranous ossification with emphasis on the processes that only occur in this type of ossification.

- The *in-silico* study of bone healing in mouth can contribute not only to a better understanding of intramembranous ossification but also to the better understanding of the ossification processes in long bones, since some biological phenomena are excluded and the remaining can be analyzed more deeply.
- The proposed model and its future improvements will aid planning dental procedures, analyzing new treatment strategies and designing enhanced dental implants. Furthermore, they may not only contribute to reduce the need for animal tests, but also to the proper experimental design for both *in-vivo* and *in-vitro* tests.
- The simulations showed the importance of considering both H-D and bFGF-dependent fibroblast apoptosis, especially for modeling intramembranous ossification.
- Hill funtions are useful for describing activation thresholds, but in furtherance of solving them inside a FEM it is important to be careful with their usage in behalf of numerical concordance.
- In the direction of improving the IOM, further experimental research is needed in order to accurately measure diffusion coefficients, cell half-life times, growth factor synthesis, consumption and degradation rates, etc. The accuracy of the simulations highly depends on using reliable data.
- In pursuance of a better understanding of the biological process of bone healing, a rigorous study about other important phenomena should be made: blood clot formation and resorption, specific growth factor synthesis and degradation, macrophage activity, and mechanically induced osteogenesis.
- As seen in Section 4, the assigned boundary conditions have an important effect on the simulation outcome. In order to extend the application of this model to the clinical practice, medical imaging techniques jointly with biomarkers assays should be developed to determine the particular characteristics of each individual and thus achieving customized, more effective therapeutical approaches.
- Mechanical loads and interstitial fluid flow have an effect on cellular differentiation, migration, proliferation and protein synthesis [73–75]. The omission of these effects in the IOM might have a limited impact on the present analysis, since in the original study Cardaropoli *et al.* [27] ensured minimal loading conditions by means of feeding the dogs with a soft pellet diet throughout the experiment. Nonetheless, indirect loading from surrounding teeth and stresses due to possible inflammatory responses will take place in the extraction site. More investigation on the

mechanobiological pathways of bone metabolism is needed in order to incorporate these phenomena into the IOM.

Mechanical loading will play an important role in future *in-silico* studies. This could lead to accurate descriptions of compromised healing situations, of the effects of dental implant loading on bone formation, and of inflammatory responses and their influence on bone healing (including the inflammatory responses caused by growth factors administration [12]).

6. Conflicts of interest

The authors declare that they have no conflicts of interest.

7. Acknowledgements

The research group would like to thank professor Liesbet Geris for her advice on topics related with the bioregulatory model and for her friendly disposition and willingness to help.

We would also like to thank the Colombian Administrative Department of Science, Technology and Innovation (COLCIENCIAS) for the financial support given to the project.

References

References

- [1] V. Luginbuehl, L. Meinel, H. P. Merkle, B. Gander, Localized delivery of growth factors for bone repair, *European Journal of Pharmaceutics and Biopharmaceutics* 58 (2) (2004) 197–208. [doi:10.1016/j.ejpb.2004.03.004](https://doi.org/10.1016/j.ejpb.2004.03.004).
- [2] S. Mitragotri, Healing sound: the use of ultrasound in drug delivery and other therapeutic applications, *Nature Reviews Drug Discovery* 4 (3) (2005) 255–260. [doi:10.1038/nrd1662](https://doi.org/10.1038/nrd1662).
- [3] M. Doblaré, J. García, M. Gómez, Modelling bone tissue fracture and healing: a review, *Engineering Fracture Mechanics* 71 (13) (2004) 1809–1840. [doi:10.1016/j.engfracmech.2003.08.003](https://doi.org/10.1016/j.engfracmech.2003.08.003).
- [4] H. Isaksson, Recent advances in mechanobiological modeling of bone regeneration, *Mechanics Research Communications* 42 (2012) 22–31. [doi:10.1016/j.mechrescom.2011.11.006](https://doi.org/10.1016/j.mechrescom.2011.11.006).
- [5] D. Lacroix, P. Prendergast, A mechano-regulation model for tissue differentiation during fracture healing: analysis of gap size and loading, *Journal of biomechanics* 35 (9) (2002) 1163–1171. [doi:10.1016/S0021-9290\(02\)00086-6](https://doi.org/10.1016/S0021-9290(02)00086-6).
- [6] M. Gomez-Benito, J. Garcia-Aznar, J. Kuiper, M. Doblaré, Influence of fracture gap size on the pattern of long bone healing: a computational study, *Journal of theoretical biology* 235 (1) (2005) 105–119. [doi:10.1016/j.jtbi.2004.12.023](https://doi.org/10.1016/j.jtbi.2004.12.023).
- [7] A. Bailon-Plaza, M. C. Van Der Meulen, A mathematical framework to study the effects of growth factor influences on fracture healing, *Journal of Theoretical Biology* 212 (2) (2001) 191–209. [doi:10.1006/jtbi.2001.2372](https://doi.org/10.1006/jtbi.2001.2372).
- [8] L. Geris, J. Vander Sloten, H. Van Oosterwyck, Connecting biology and mechanics in fracture healing: an integrated mathematical modeling framework for the study of nonunions, *Biomechanics and modeling in mechanobiology* 9 (6) (2010) 713–724. [doi:10.1007/s10237-010-0208-8](https://doi.org/10.1007/s10237-010-0208-8).
- [9] J. Garcia-Aznar, J. Kuiper, M. Gómez-Benito, M. Doblaré, J. Richardson, Computational simulation of fracture healing: influence of interfragmentary movement on the callus growth, *Journal of biomechanics* 40 (7) (2007) 1467–1476. [doi:10.1016/j.jbiomech.2006.06.013](https://doi.org/10.1016/j.jbiomech.2006.06.013).
- [10] P. Pivonka, S. V. Komarova, Mathematical modeling in bone biology: From intracellular signaling to tissue mechanics, *Bone* 47 (2) (2010) 181–189. [doi:10.1016/j.bone.2010.04.601](https://doi.org/10.1016/j.bone.2010.04.601).
- [11] S. V. Komarova, R. J. Smith, S. J. Dixon, S. M. Sims, L. M. Wahl, Mathematical model predicts a critical role for osteoclast autocrine regulation in the control of bone remodeling, *Bone* 33 (2) (2003) 206–215. [doi:10.1016/S8756-3282\(03\)00157-1](https://doi.org/10.1016/S8756-3282(03)00157-1).
- [12] F. O. Ribeiro, M. J. Gómez-Benito, J. Folgado, P. R. Fernandes, J. M. García-Aznar, In silico mechano-chemical model of bone healing for the regeneration of critical defects: the effect of bmp-2, *PLoS one* 10 (6) (2015) e0127722. [doi:10.1371/journal.pone.0127722](https://doi.org/10.1371/journal.pone.0127722).
- [13] L. Geris, A. Gerisch, J. Vander Sloten, R. Weiner, H. Van Oosterwyck, Angiogenesis in bone fracture healing: a bioregulatory model, *Journal of theoretical biology* 251 (1) (2008) 137–158. [doi:10.1016/j.jtbi.2007.11.008](https://doi.org/10.1016/j.jtbi.2007.11.008).
- [14] V. Peiffer, A. Gerisch, D. Vandepitte, H. Van Oosterwyck, L. Geris, A hybrid bioregulatory model of angiogenesis during bone fracture healing, *Biomechanics and modeling in mechanobiology* 10 (3) (2011) 383–395. [doi:10.1007/s10237-010-0241-7](https://doi.org/10.1007/s10237-010-0241-7).

[15] A. Carlier, L. Geris, K. Bentley, G. Carmeliet, P. Carmeliet, H. Van Oosterwyck, Mosaic: a multiscale model of osteogenesis and sprouting angiogenesis with lateral inhibition of endothelial cells, *PLOS: Computational Biology* (2012). [doi:10.1371/journal.pcbi.1002724](https://doi.org/10.1371/journal.pcbi.1002724).

[16] L. Zhang, M. Richardson, P. Mendis, Role of chemical and mechanical stimuli in mediating bone fracture healing, *Clinical and Experimental Pharmacology and Physiology* 39 (8) (2012) 706–710. [doi:10.1111/j.1440-1681.2011.05652.x](https://doi.org/10.1111/j.1440-1681.2011.05652.x).

[17] L. C. Gerstenfeld, D. M. Cullinane, G. L. Barnes, D. T. Graves, T. A. Einhorn, Fracture healing as a post-natal developmental process: Molecular, spatial, and temporal aspects of its regulation, *Journal of cellular biochemistry* 88 (5) (2003) 873–884. [doi:10.1002/jcb.10435](https://doi.org/10.1002/jcb.10435).

[18] G. L. Barnes, P. J. Kostenuik, L. C. Gerstenfeld, T. A. Einhorn, Growth factor regulation of fracture repair, *Journal of Bone and Mineral Research* 14 (11) (1999) 1805–1815. [doi:10.1359/jbmr.1999.14.11.1805](https://doi.org/10.1359/jbmr.1999.14.11.1805).

[19] V. I. Sikavitsas, J. S. Temenoff, A. G. Mikos, Biomaterials and bone mechanotransduction, *Biomaterials* 22 (19) (2001) 2581–2593. [doi:10.1016/S0142-9612\(01\)00002-3](https://doi.org/10.1016/S0142-9612(01)00002-3).

[20] C. Ferguson, E. Alpern, T. Miclau, J. A. Helms, Does adult fracture repair recapitulate embryonic skeletal formation?, *Mechanisms of development* 87 (1) (1999) 57–66. [doi:10.1016/S0925-4773\(99\)00142-2](https://doi.org/10.1016/S0925-4773(99)00142-2).

[21] A. Vortkamp, S. Pathi, G. M. Peretti, E. M. Caruso, D. J. Zaleske, C. J. Tabin, Recapitulation of signals regulating embryonic bone formation during postnatal growth and in fracture repair, *Mechanisms of development* 71 (1) (1998) 65–76. [doi:10.1016/S0925-4773\(97\)00203-7](https://doi.org/10.1016/S0925-4773(97)00203-7).

[22] A. Reed, C. Joyner, S. Isefuku, H. Brownlow, A. Simpson, Vascularity in a new model of atrophic nonunion, *Journal of Bone & Joint Surgery, British Volume* 85 (4) (2003) 604–610. [doi:10.1302/0301-620X.85B4.12944](https://doi.org/10.1302/0301-620X.85B4.12944).

[23] T. Kokubu, D. J. Hak, S. J. Hazelwood, A. H. Reddi, Development of an atrophic nonunion model and comparison to a closed healing fracture in rat femur, *Journal of orthopaedic research* 21 (3) (2003) 503–510. [doi:10.1016/S0736-0266\(02\)00209-7](https://doi.org/10.1016/S0736-0266(02)00209-7).

[24] L. J. Harrison, J. L. Cunningham, L. Strömberg, A. E. Goodship, Controlled induction of a pseudarthrosis: a study using a rodent model, *Journal of orthopaedic trauma* 17 (1) (2003) 11–21.

[25] J. Frommer, M. R. Margolies, Contribution of meckel's cartilage to ossification of the mandible in mice, *Journal of dental research* 50 (5) (1971) 1260–1267. [doi:10.1177/00220345710500052801](https://doi.org/10.1177/00220345710500052801).

[26] S. Shibata, Y. Sakamoto, T. Yokohama-Tamaki, G. Murakami, B. H. Cho, Distribution of matrix proteins in perichondrium and periosteum during the incorporation of meckel's cartilage into ossifying mandible in midterm human fetuses: An immunohistochemical study, *The Anatomical Record* 297 (7) (2014) 1208–1217. [doi:10.1002/ar.22911](https://doi.org/10.1002/ar.22911).

[27] G. Cardaropoli, M. Araujo, J. Lindhe, Dynamics of bone tissue formation in tooth extraction sites, *Journal of clinical periodontology* 30 (9) (2003) 809–818. [doi:10.1034/j.1600-051X.2003.00366.x](https://doi.org/10.1034/j.1600-051X.2003.00366.x).

[28] M. G. Araujo, J. Lindhe, Dimensional ridge alterations following tooth extraction. an experimental study in the dog, *Journal of clinical periodontology* 32 (2) (2005) 212–218. [doi:10.1111/j.1600-051X.2005.00642.x](https://doi.org/10.1111/j.1600-051X.2005.00642.x).

[29] Y. Kuboki, F. Hashimoto, K. Ishibashi, Time-dependent changes of collagen crosslinks in the socket after tooth extraction in rabbits, *Journal of Dental Research* 67 (6) (1988) 944–948. [doi:10.1177/00220345880670061101](https://doi.org/10.1177/00220345880670061101).

[30] H. Simpson, Experimental investigation into the healing of extraction wounds in macacus rhesus monkeys., *Journal of oral surgery, anesthesia, and hospital dental service* 18 (1960) 391.

[31] M. H. Amler, The time sequence of tissue regeneration in human extraction wounds, *Oral Surgery, Oral Medicine, Oral Pathology* 27 (3) (1969) 309–318. [doi:10.1016/0030-4220\(69\)90357-0](https://doi.org/10.1016/0030-4220(69)90357-0).

[32] F. R. Christopher, A histological study of bone healing in relation to the extraction of teeth, 1941.

[33] J. E. Davies, Understanding peri-implant endosseous healing, *Journal of dental education* 67 (8) (2003) 932–949.

[34] S. Chandrasekhar, A. K. Harvey, Modulation of pdgf mediated osteoblast chemotaxis by leukemia inhibitory factor lif, *Journal of cellular physiology* 169 (3) (1996) 481–490. [doi:10.1002/\(SICI\)1097-4652\(199612\)169:3<481::AID-JCP8>3.0.CO;2-K](https://doi.org/10.1002/(SICI)1097-4652(199612)169:3<481::AID-JCP8>3.0.CO;2-K).

[35] I. F.-T. Hernandez-Gil, M. A. Gracia, M. del Canto Pingarrn, L. B. Jerez, Physiological bases of bone regeneration i. histology and physiology of bone tissue, *Med Oral* 11 (2006) E47–51.

[36] W.-Y. Li, S. S. Chong, E. Y. Huang, T.-L. Tuan, Plasminogen activator/plasmin system: a major player in wound healing?, *Wound repair and regeneration* 11 (4) (2003) 239–247. [doi:10.1046/j.1524-475X.2003.11402.x](https://doi.org/10.1046/j.1524-475X.2003.11402.x).

[37] I. Aukhil, Biology of wound healing, *Periodontology 2000* 22 (1) (2000) 44–50. [doi:10.1034/j.1600-0757.2000.2220104.x](https://doi.org/10.1034/j.1600-0757.2000.2220104.x).

[38] J. Vanegas-Acosta, D. Garzón-Alvarado, et al., A finite element method approach for the mechanobiological modeling of the osseointegration of a dental implant, *Computer Methods and Programs in Biomedicine* 101 (3) (2011) 297–314. [doi:10.1016/j.cmpb.2010.11.007](https://doi.org/10.1016/j.cmpb.2010.11.007).

[39] N. Ferrara, T. Davis-Smyth, The biology of vascular endothelial growth factor, *Endocrine reviews* 18 (1) (1997) 4–25.

[40] C. W. Pugh, P. J. Ratcliffe, Regulation of angiogenesis by hypoxia: role of the hif system, *Nature medicine* 9 (6) (2003) 677–684. [doi:10.1038/nm0603-677](https://doi.org/10.1038/nm0603-677).

[41] C. Maes, G. Carmeliet, E. Schipani, Hypoxia-driven pathways in bone development, regeneration and disease, *Nature Reviews Rheumatology* 8 (6) (2012) 358–366. [doi:10.1038/nrrheum.2012.36](https://doi.org/10.1038/nrrheum.2012.36).

[42] D. Komatsu, M. Hadjiaargyrou, Activation of the transcription factor hif-1 and its target genes, vegf, ho-1, inos, during fracture repair, *Bone* 34 (4) (2004) 680–688. [doi:10.1016/j.bone.2003.12.024](https://doi.org/10.1016/j.bone.2003.12.024).

[43] M. Hirao, N. Tamai, N. Tsumaki, H. Yoshikawa, A. Myoui, Oxygen tension regulates chondrocyte differentiation and function during endochondral ossification, *Journal of Biological Chemistry* 281 (41) (2006) 31079–31092. [doi:10.1074/jbc.M602296200](https://doi.org/10.1074/jbc.M602296200).

[44] F. Long, Building strong bones: molecular regulation of the osteoblast lineage, *Nature reviews Molecular cell biology* 13 (1) (2012) 27–38. [doi:10.1038/nrm3254](https://doi.org/10.1038/nrm3254).

[45] K. Anselme, Osteoblast adhesion on biomaterials, *Biomaterials* 21 (7) (2000) 667–681. [doi:10.1016/S0142-9612\(99\)00242-2](https://doi.org/10.1016/S0142-9612(99)00242-2).

[46] L. Olsen, J. A. Sherratt, P. K. Maini, F. Arnold, A mathematical model for the capillary endothelial cell-extracellular matrix interactions in wound-healing angiogenesis, *Mathematical Medicine and Biology* 14 (4) (1997) 261–281. [doi:10.1093/imammb/14.4.261](https://doi.org/10.1093/imammb/14.4.261).

[47] A. Carlier, L. Geris, N. van Gastel, G. Carmeliet, H. Van Oosterwyck, Oxygen as a critical determinant of bone fracture healing - a multiscale model, *Journal of theoretical biology* 365 (2015) 247–264. [doi:10.1016/j.jtbi.2014.10.012](https://doi.org/10.1016/j.jtbi.2014.10.012).

[48] R. Strehl, A. Sokolov, D. Kuzmin, S. Turek, A flux-corrected finite element method for chemotaxis problems, *Computational Methods in Applied Mathematics* 10 (2) (2010) 219–232. [doi:10.2478/cmam-2010-0013](https://doi.org/10.2478/cmam-2010-0013).

[49] R. Strehl, A. Sokolov, D. Kuzmin, D. Horstmann, S. Turek, A positivity-preserving finite element method for chemotaxis problems in 3d, *Journal of Computational and Applied Mathematics* 239 (2013) 290–303. [doi:10.1016/j.cam.2012.09.041](https://doi.org/10.1016/j.cam.2012.09.041).

[50] C. T. BRIGHTON, A. G. KREBS, Oxygen tension of healing fractures in the rabbit, *The Journal of Bone & Joint Surgery* 54 (2) (1972) 323–332.

[51] W. L. Grayson, F. Zhao, B. Bunnell, T. Ma, Hypoxia enhances proliferation and tissue formation of human mesenchymal stem cells, *Biochemical and biophysical research communications* 358 (3) (2007) 948–953. [doi:10.1016/j.bbrc.2007.05.054](https://doi.org/10.1016/j.bbrc.2007.05.054).

[52] H.-J. Chae, S.-C. Kim, K.-S. Han, S.-W. Chae, N.-H. An, H.-M. Kim, H.-H. Kim, Z.-H. Lee, H.-R. Kim, Hypoxia induces apoptosis by caspase activation accompanying cytochrome c release from mitochondria in mc3t3e1 osteoblasts. p38 mapk is related in hypoxia-induced apoptosis, *Immunopharmacology and immunotoxicology* 23 (2) (2001) 133–152. [doi:10.1081/IPH-100103855](https://doi.org/10.1081/IPH-100103855).

[53] P. Fraisl, M. Mazzone, T. Schmidt, P. Carmeliet, Regulation of angiogenesis by oxygen and metabolism, *Developmental cell* 16 (2) (2009) 167–179. [doi:10.1016/j.devcel.2009.01.003](https://doi.org/10.1016/j.devcel.2009.01.003).

[54] Y. Akasaka, I. Ono, T. Kamiya, Y. Ishikawa, T. Kinosita, S. Ishiguro, T. Yokoo, R. Imaizumi, N. Inomata, K. Fujita, et al., The mechanisms underlying fibroblast apoptosis regulated by growth factors during wound healing, *The Journal of pathology* 221 (3) (2010) 285–299. [doi:10.1002/path.2710](https://doi.org/10.1002/path.2710).

[55] L. Schweigerer, G. Neufeld, J. Friedman, J. A. Abraham, J. C. Fiddes, D. Gospodarowicz, Capillary endothelial cells express basic fibroblast growth factor, a mitogen that promotes their own growth, *Nature* 325 (6101) (1987) 257–259. [doi:10.1038/325257a0](https://doi.org/10.1038/325257a0).

[56] I. Vlodavsky, J. Folkman, R. Sullivan, R. Friedman, R. Ishai-Michaeli, J. Sasse, M. Klagsbrun, Endothelial cell-derived basic fibroblast growth factor: synthesis and deposition into subendothelial extracellular matrix, *Proceedings of the National Academy of Sciences* 84 (8) (1987) 2292–2296.

[57] G. Seghezzi, S. Patel, C. J. Ren, A. Gualandris, G. Pintucci, E. S. Robbins, R. L. Shapiro, A. C. Gallopoway, D. B. Rifkin, P. Mignatti, Fibroblast growth factor-2 (fgf-2) induces vascular endothelial growth

factor (vegf) expression in the endothelial cells of forming capillaries: an autocrine mechanism contributing to angiogenesis, *The Journal of cell biology* 141 (7) (1998) 1659–1673. [doi:10.1083/jcb.141.7.1659](https://doi.org/10.1083/jcb.141.7.1659).

[58] S. Mehta, J. T. Watson, Platelet rich concentrate: basic science and current clinical applications, *Journal of orthopaedic trauma* 22 (6) (2008) 432–438. [doi:10.1097/BOT.0b013e31817e793f](https://doi.org/10.1097/BOT.0b013e31817e793f).

[59] R. E. Marx, Platelet-rich plasma (prp): what is prp and what is not prp?, *Implant dentistry* 10 (4) (2001) 225–228.

[60] J. Street, M. Bao, S. Bunting, F. V. Peale, N. Ferrara, H. Steinmetz, J. Hoeffel, J. L. Cleland, A. Daugherty, N. van Bruggen, et al., Vascular endothelial growth factor stimulates bone repair by promoting angiogenesis and bone turnover, *Proceedings of the National Academy of Sciences* 99 (15) (2002) 9656–9661. [doi:10.1073/pnas.152324099](https://doi.org/10.1073/pnas.152324099).

[61] H. Mayer, H. Bertram, W. Lindenmaier, T. Korff, H. Weber, H. Weich, Vascular endothelial growth factor (vegf-a) expression in human mesenchymal stem cells: Autocrine and paracrine role on osteoblastic and endothelial differentiation, *Journal of cellular biochemistry* 95 (4) (2005) 827–839. [doi:10.1002/jcb.20462](https://doi.org/10.1002/jcb.20462).

[62] M. Rupnick, C. Stokes, S. Williams, D. Lauffenburger, Quantitative analysis of random motility of human microvessel endothelial cells using a linear under-agarose assay., *Laboratory investigation; a journal of technical methods and pathology* 59 (3) (1988) 363–372.

[63] L. Olsen, J. A. Sherratt, P. K. Maini, A mechanochemical model for adult dermal wound contraction: on the permanence of the contracted tissue displacement profile, *Journal of theoretical biology* 177 (2) (1995) 113–128.

[64] C. McCulloch, E. Nemeth, B. Lowenberg, A. Melcher, Paravascular cells in endosteal spaces of alveolar bone contribute to periodontal ligament cell populations, *The Anatomical record* 219 (3) (1987) 233–242. [doi:10.1002/ar.1092190304](https://doi.org/10.1002/ar.1092190304).

[65] C. McCulloch, A. Melcher, Cell density and cell generation in the periodontal ligament of mice, *American Journal of Anatomy* 167 (1) (1983) 43–58. [doi:10.1002/aja.1001670105](https://doi.org/10.1002/aja.1001670105).

[66] V. Kingsmill, C. Gray, D. Moles, A. Boyde, Cortical vascular canals in human mandible and other bones, *Journal of dental research* 86 (4) (2007) 368–372. [doi:10.1177/154405910708600413](https://doi.org/10.1177/154405910708600413).

[67] S. Young, J. D. Kretlow, C. Nguyen, A. G. Bashoura, L. S. Baggett, J. A. Jansen, M. Wong, A. G. Mikos, Microcomputed tomography characterization of neovascularization in bone tissue engineering applications, *Tissue Engineering Part B: Reviews* 14 (3) (2008) 295–306. [doi:10.1089/ten.teb.2008.0153](https://doi.org/10.1089/ten.teb.2008.0153).

[68] A. Chevrier, C. Hoemann, J. Sun, M. Buschmann, Chitosan–glycerol phosphate/blood implants increase cell recruitment, transient vascularization and subchondral bone remodeling in drilled cartilage defects, *Osteoarthritis and Cartilage* 15 (3) (2007) 316–327. [doi:10.1016/j.joca.2006.08.007](https://doi.org/10.1016/j.joca.2006.08.007).

[69] W.-L. Lin, C. A. McCulloch, M.-I. Cho, Differentiation of periodontal ligament fibroblasts into osteoblasts during socket healing after tooth extraction in the rat, *The Anatomical Record* 240 (4) (1994) 492–506. [doi:10.1002/ar.1092400407](https://doi.org/10.1002/ar.1092400407).

[70] C. K. Hee, M. A. Jonikas, S. B. Nicoll, Influence of three-dimensional scaffold on the expression of osteogenic differentiation markers by human dermal fibroblasts, *Biomaterials* 27 (6) (2006) 875–884. [doi:10.1016/j.biomaterials.2005.07.004](https://doi.org/10.1016/j.biomaterials.2005.07.004).

[71] M. C. Meikle, S. Bord, R. M. Hembry, J. Compston, P. I. Croucher, J. J. Reynolds, Human osteoblasts in culture synthesize collagenase and other matrix metalloproteinases in response to osteotropic hormones and cytokines, *Journal of cell science* 103 (4) (1992) 1093–1099.

[72] P. A. Prokharau, F. J. Vermolen, J. M. García-Aznar, A mathematical model for cell differentiation, as an evolutionary and regulated process, *Computer methods in biomechanics and biomedical engineering* 17 (10) (2014) 1051–1070. [doi:10.1080/10255842.2012.736503](https://doi.org/10.1080/10255842.2012.736503).

[73] A. Gefen, *Cellular and Biomolecular Mechanics and Mechanobiology*, Springer, 2011. [doi:10.1007/978-3-642-14218-5](https://doi.org/10.1007/978-3-642-14218-5).

[74] Z. Thompson, T. Miclau, D. Hu, J. A. Helms, A model for intramembranous ossification during fracture healing, *Journal of Orthopaedic Research* 20 (5) (2002) 1091–1098. [doi:10.1016/S0733-0266\(02\)00017-7](https://doi.org/10.1016/S0733-0266(02)00017-7).

[75] P. Prendergast, S. Checa, D. Lacroix, Computational models of tissue differentiation, in: *Computational modeling in biomechanics*, Springer, 2010, pp. 353–372. [doi:10.1007/978-90-481-3575-2_12](https://doi.org/10.1007/978-90-481-3575-2_12).

Appendix A. Non-dimensional parameters

Equations 4–12 were non-dimensionalized as proposed by Geris *et al.* [13], but as mentioned before, we made

some modifications, in order improve the robustness of the FEM implementation. The scalings are the following:

$$\begin{aligned}\tilde{t} &= \frac{t}{T}, & \tilde{x}_h &= \frac{x_h}{L}, & \tilde{c}_i &= \frac{c_i}{c_0}, & \tilde{c}_v &= \frac{c_v}{c_{v,0}}, \\ \tilde{m}_j &= \frac{m_j}{m_0}, & \tilde{m}_v &= \frac{m_v}{m_{v,0}}, & \tilde{g}_k &= \frac{g_k}{g_0}\end{aligned}\tag{A.1}$$

Where x_h are the coordinates that define the position of a point (r and z for the axisymmetric model); $i = m, f, b$; $j = m, b$ and $k = b, v$. The characteristic scales for the variables were chosen exactly the same as in [13], except for $c_{v,0}$ (which was changed to avoid great differences of order of magnitude), $m_{v,0}$ (which was changed automatically when adopting the vascularization model of Olsen *et al.* [46]) and L (which was chosen using optimization algorithm). The characteristic scales are $T = 1$ day, $L = 1$ mm, $m_0 = 0.1$ g/ml, $g_0 = 100$ ng/ml, $c_0 = 10^6$ cells/ml and $c_{v,0} = 10^2$ cells/ml. Since $T = 1$ mm, the alveolar geometry can be modeled in mm and it is not necessary to scale it.

Table A.3: Adimensional parameters obtained for the calculations of this study (excluding differentiation parameters - Table A.4). The sub-index x of the parameters in the first column is to be replaced with the letters of the first row. Calculation of D_x ; $C_{x,CT}$; $C_{x,HT}$; and A_x with values of first 8 rows is explained in [13]

	m	f	b	v	Description
For cells					
\tilde{D}_{hx}	0.1715	0.00147*		0.1417	Diffusivity parameter 1
\tilde{K}_{hx}	0.25			1	Diffusivity parameter 2
\tilde{C}_{kCTx}	0.49	4.9		0.37485	Chemotaxis parameter 1
\tilde{K}_{kCTx}	0.1	0.1		0.025	Chemotaxis parameter 2
\tilde{C}_{kHTx}	0.04165			0.03**	Haptotaxis parameter 1
\tilde{K}_{kHTx}	0.5				Haptotaxis parameter 2
\tilde{A}_{x0}	1.01	0.202	0.202	0.202	Proliferation rate param. 1
\tilde{K}_x	0.1	0.1	0.1	0.1	Proliferation rate param. 1
$\tilde{\alpha}_x$	1	1	1	1	Saturation for proliferation
$\tilde{d}_{x,constant}$				0.1	Constant apoptosis rate
$\tilde{d}_{x,hyp}$	10	10	10		H-D apoptosis rate
$\tilde{H}_{hyp,x}$	0.04167	0.1875	0.167		Threshold for H-D apoptosis
$\tilde{d}_{x,bFGF}$		0.45			bFGF-dependent apoptosis rate
$\tilde{H}_{bFGF,x}$		0.92			Threshold for bFGF-dependent apoptosis
For extra-cellular matrices					
\tilde{P}_{xs}		0.2	2	1	Synthesis rate
$\tilde{\kappa}_x$		1	1	1	Maximum matrix density
\tilde{Q}_x		1.5			Resorption rate
For growth factors					
\tilde{D}_{gx}			0.06125	6.125	Diffusivity
\tilde{G}_{gbx}			1000		\tilde{g}_b production rate
\tilde{G}_{gvx}			5×10^{-5}		\tilde{g}_v production rate
\tilde{H}_{gx}			1	0.03	Threshold for growth factor production
\tilde{d}_{gx}		100	30		Decay rate
\tilde{d}_{gvx}			20		Consumption rate of \tilde{g}_v
$\tilde{\epsilon}_{hyp,x}$	1	1	1		H-D \tilde{g}_v production rate
$\tilde{K}_{hyp,x}$	0.167	0.375	0.33		Threshold for H-D \tilde{g}_v production
$\tilde{\epsilon}_{clot}$		30			\tilde{g}_v production rate by BC
\tilde{K}_{clot}		0.350			Threshold for \tilde{g}_v production by BC

*Value for constant diffusivity of fibroblasts (ignore \tilde{K}_{hf})

**Value for constant haptotaxis parameter of endothelial cells (ignore $\tilde{K}_{v,HT}$)

Table A.4: Non-dimensional differentiation parameters used for the simulations.

Parameter	Value	Description
\tilde{Y}_{11}	20	MSC to osteoblast differentiation rate 1 (see [13])
\tilde{H}_{11}	0.1	MSC to osteoblast differentiation parameter 1 (see [13])
\tilde{Y}_{12}	2.3	MSC to osteoblast differentiation rate 2 (see [13])
\tilde{H}_{12}	0.1	MSC to osteoblast differentiation parameter 2 (see [13])
\tilde{I}_v	0.667	Minimum vascularization needed for $c_m \rightarrow c_b$ differentiation
\tilde{F}_{mf}	0.01	MSC to fibroblast differentiation rate
\tilde{F}_{bo}	0.01	Osteoblast to osteocyte differentiation rate